I. SUPPLEMENTARY FIGURES

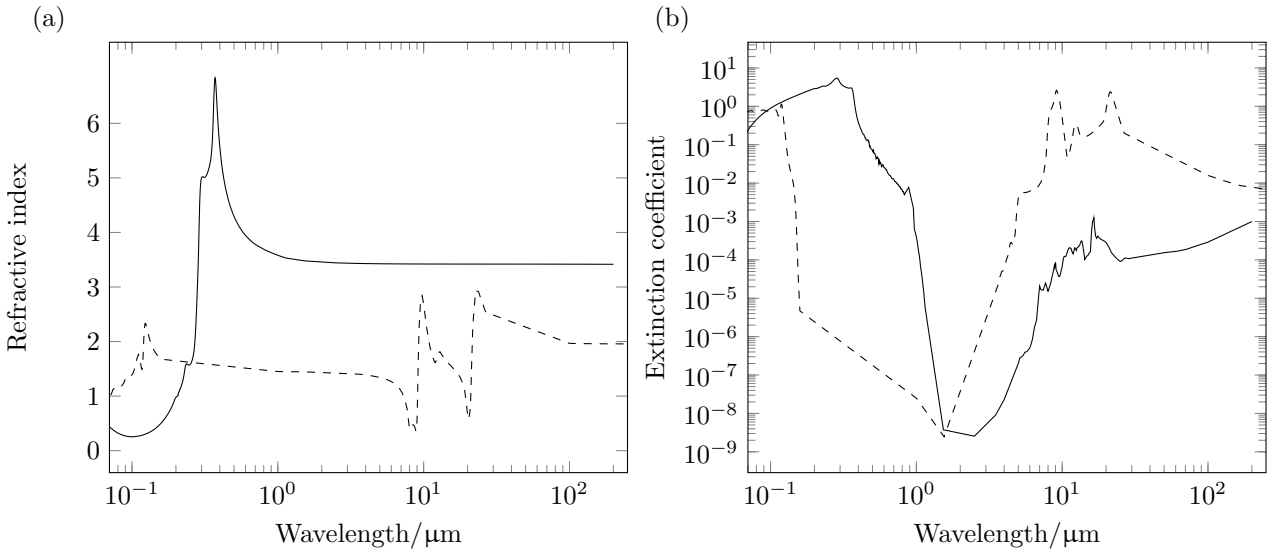

Supplementary Figure 1. **Spectral properties of silicon and silica.** Refractive indices (a) and absorption coefficients (b) for silicon (solid) and glass silica (dashed) as a function of the optical wavelength. Data are for bulk materials as found in Ref. [1]. At wavelengths where absorption data is available and refractive index measurements are absent, the latter, which varies slowly, is found by linear interpolation. Due to lack of tabulated data near the absorption minima, we have included values from recent absorption measurements [2, 3]. The depicted spectra cover all relevant blackbody wavelengths for temperatures of the order of 10^3 K. We determine the static value of the dielectric function, as used to estimate the effect of collisions with background gas, by the refractive index value at the longest available wavelength.

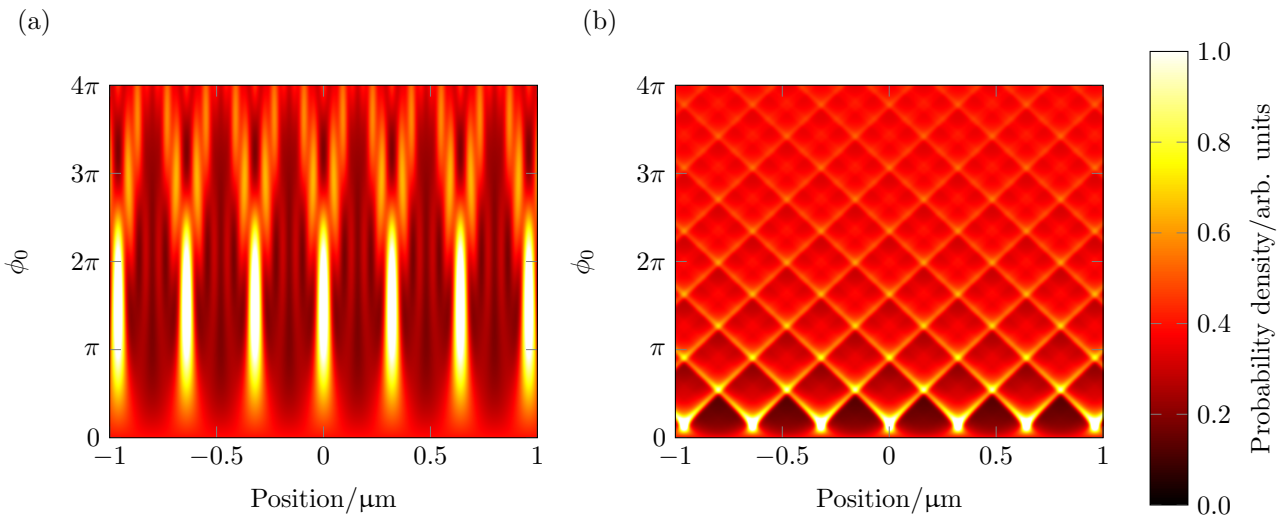

Supplementary Figure 2. **Quantum and classical fringe patterns.** (a) Quantum and (b) classical fringe patterns for a grating period $d = 355$ nm/2 with $t_2 = 1.6t_T$ as we vary the maximum phase modulation ϕ_0. The initial particle localization is $\sigma_x = 10$ nm and the free-flight time before the grating is $t_1 = 2t_T$ with $t_T = 80$ ms.

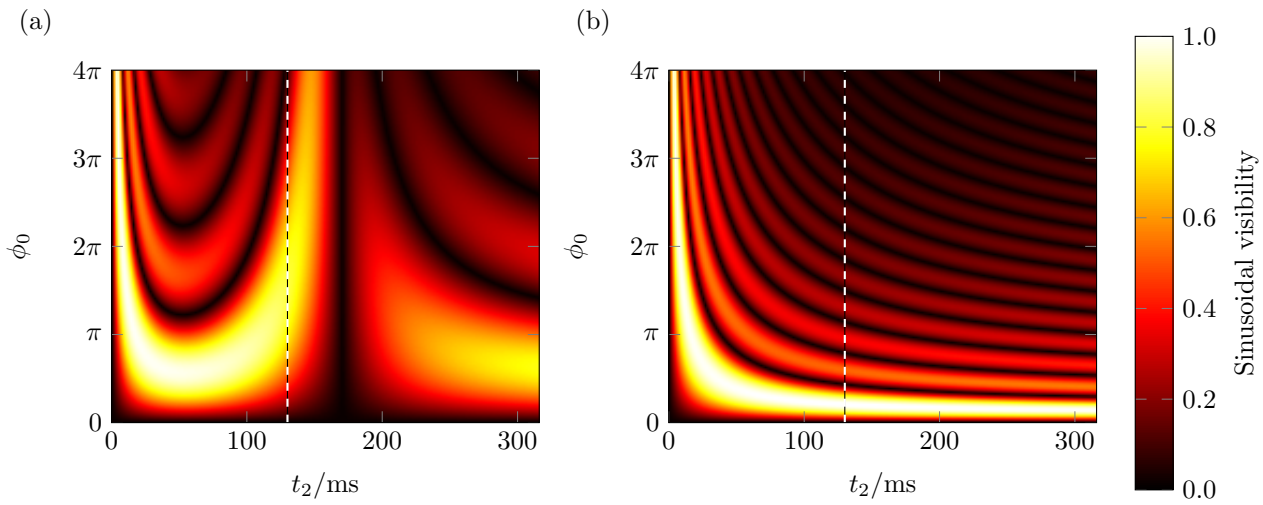

Supplementary Figure 3. **Quantum and classical sinusoidal visibilities.** (a) Quantum and (b) classical sinusoidal visibilities for the parameters mentioned in the text, with varying grating phase ϕ_0 and time t_2, for fixed $t_1 = 2t_T$. The vertical line shows the fixed time $t_2 = 1.6t_T$ for which we plot the visibilities as a function of phase in Fig. 3.

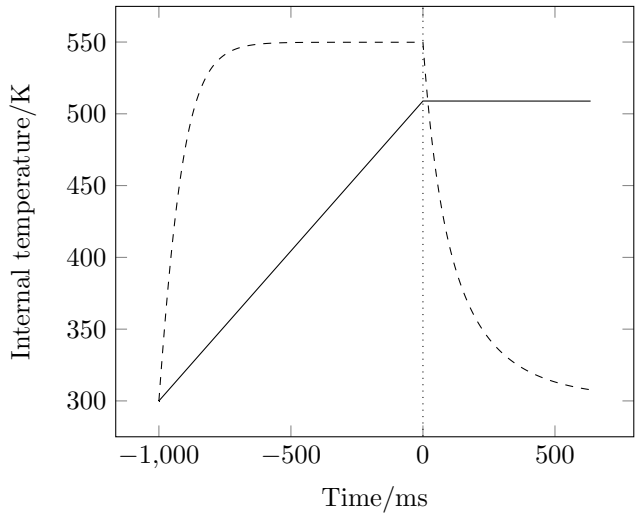

Supplementary Figure 4. **Internal heating and cooling of silicon and silica nanospheres.** Silicon (solid) and silica (dashed) nanospheres of 10^6 amu are exposed in the interval $(-1000\,\mathrm{ms}, 0)$ to light at wavelength 1550 nm focused with a 0.8 NA lens with intensity $I = 90\,\mathrm{mW/\mu m^2}$ (silicon), $I = 300\,\mathrm{mW/\mu m^2}$ (silica) chosen to yield a trap frequency $\nu_\mathrm{M} = 200\,\mathrm{kHz}$. The silica particle reaches equilibrium temperature while the silicon particle undergoes constant heating, with an estimated equilibrium temperature of 1600 K. The enhanced infrared emissivity of silica gives rise to significant cooling after release, whereas silicon is almost perfectly isolated.

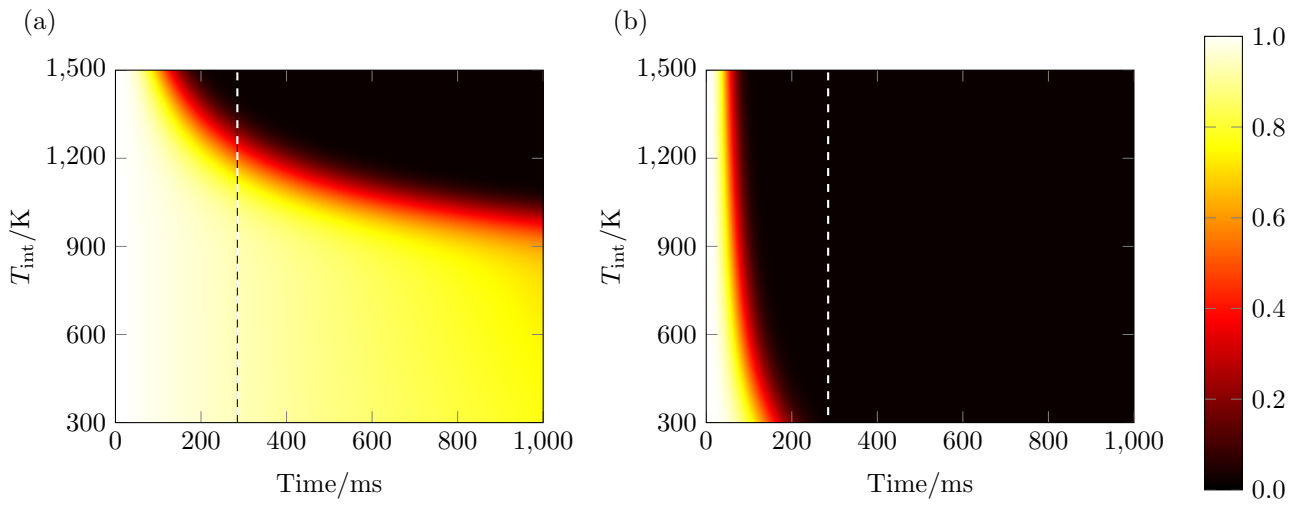

Supplementary Figure 5. **Reduction in visibility from decoherence for silicon and silica.** Reduction of the sinusoidal interference fringe visibility due to decoherence as a function of initial internal temperature and total time $t = t_1 + t_2$, with the ratio $t_1/t_2 = 2/1.6$ as in our proposed experiment, for (a) silicon and (b) silica nanospheres. We assume a fixed environmental temperature of $T_{\text{env}} = 300\,\text{K}$ and a gas pressure of $p_g = 10^{-10}\,\text{mbar}$. The vertical dashed line corresponds to $t_1 + t_2 = 3.6t_T$, which is the duration of the proposed interference experiment. We see clearly that silica exhibits significant decoherence due to thermal emission. Decoherence due to collisions with background gas is only significant for times after approximately 500 ms.

II. SUPPLEMENTARY NOTES

Supplementary Note 1: Dielectric properties of nanospheres

We summarize the important aspects of the linear interaction between spherical nanoparticles and electromagnetic fields. Given an electromagnetic wave of frequency $\omega = 2\pi c/\lambda$, the linear response of a dielectric nanosphere of radius $R \ll \lambda$ is described by the complex polarizability, or susceptibility [4],

$$\alpha = 4\pi\varepsilon_0 R^3 \frac{\varepsilon(\omega) - 1}{\varepsilon(\omega) + 2}. \qquad \text{(Supplementary Equation 1)}$$

The relative permittivity is given by the square of the complex refractive index of the sphere material, $\varepsilon = n^2$. We consider spheres which consist of many atoms, using refractive index data of the bulk material.

The real part of the susceptibility determines the optical potential and dipole force acting on the particle in the presence of the standing-wave field $\boldsymbol{E}(x,t)$,

$$V(x,t) = -\frac{1}{4}\mathrm{Re}\{\alpha\}\,|\boldsymbol{E}(x,t)|^2 = -\frac{2\pi R^3}{c} I(x,t)\,\mathrm{Re}\left\{\frac{\varepsilon(\omega)-1}{\varepsilon(\omega)+2}\right\}. \qquad \text{(Supplementary Equation 2)}$$

For a laser pulse of input power $P_\mathrm{G}(t)$ and spot area a_G that is reflected off a mirror to form a standing wave, we find the intensity $I(x,t) = 4P_\mathrm{G}(t)\cos^2(2\pi x/\lambda)/a_\mathrm{G}$ in the center of the spot. The optical dipole potential is the basis of the phase grating effect of such a standing-wave pulse, as the potential (Supplementary Equation 2) gives rise to the eikonal phase

$$\phi(x) = -\frac{1}{\hbar}\int \mathrm{d}t\, V(x,t) = \frac{2\mathrm{Re}\{\alpha\}\,E_\mathrm{G}}{\hbar c\varepsilon_0 a_\mathrm{G}}\cos^2\left(\frac{2\pi x}{\lambda}\right) \equiv \phi_0\cos^2\left(\frac{2\pi x}{\lambda}\right), \qquad \text{(Supplementary Equation 3)}$$

with $E_\mathrm{G} = \int \mathrm{d}t\, P_\mathrm{G}(t)$ the pulse energy. The phase represents the classical action accumulated by a particle when illuminated by a standing-wave pulse in the Raman–Nath regime, where the laser pulse is sufficiently short (and weak) and where the particle is approximately at standstill [5, 6]. This periodic phase modulation of the motional quantum state of the particle gives rise to matter-wave interference, and it is the defining property of a phase grating.

The imaginary part of the susceptibility (Supplementary Equation 1) determines the light absorption power $P_\mathrm{abs}(x,t) = \sigma_\mathrm{abs} I(x,t)$, with the absorption cross section $\sigma_\mathrm{abs} = \omega\mathrm{Im}\{\alpha\}/c\varepsilon_0$. The average number of photons absorbed from the standing-wave pulse then reads as $n(x) = n_0\cos^2(2\pi x/\lambda) \equiv 2\beta\phi(x)$, introducing the material parameter

$$\beta = \frac{n_0}{2\phi_0} = \frac{\mathrm{Im}\{\alpha\}}{\mathrm{Re}\{\alpha\}} = \frac{3\,\mathrm{Im}\{\varepsilon(\omega)\}}{|\varepsilon(\omega)|^2 + \mathrm{Re}\{\varepsilon(\omega)\} - 2}. \qquad \text{(Supplementary Equation 4)}$$

Additional radiation pressure is related to the elastic dipole scattering of standing-wave photons into free space. The corresponding Rayleigh scattering cross-section, which is of higher order in R/λ than the absorption, reads as $\sigma_\mathrm{sca} = (2\pi/\lambda)^4 |\alpha|^2/6\pi\varepsilon_0^2$. To quantify the number of scattered photons, $n_\mathrm{sca}(x) \equiv 2\eta\phi(x)$, we introduce the material- and size-dependent parameter

$$\eta = \left(\frac{2\pi}{\lambda}\right)^3 \frac{|\alpha|^2}{6\pi\varepsilon_0 \mathrm{Re}\{\alpha\}} = \frac{2}{3}\left(\frac{2\pi R}{\lambda}\right)^3 \frac{|\varepsilon(\omega)-1|^2}{|\varepsilon(\omega)|^2 + \mathrm{Re}\{\varepsilon(\omega)\} - 2}. \qquad \text{(Supplementary Equation 5)}$$

Both absorption and Rayleigh scattering are incoherent additions to the conservative particle-light interaction given by (Supplementary Equation 2) since they induce momentum diffusion. Hence, we require $\beta, \eta \ll 1$ for a standing-wave field to properly function as a pure phase grating [7, 8]. This is indeed the case for the choice of parameters considered in the main text. Using the spectral data for silicon and crystalline silica from [1] at the grating wavelength $\lambda = \lambda_\mathrm{G} = 355\,\mathrm{nm}$ (see Supplementary Figure 1), we find $\beta = 0.06$ and $\eta = 6\times10^{-4}$ for $m = 10^6\,\mathrm{amu}$.

The correct assessment of radiative decoherence and internal heating and cooling requires knowledge about the spectral absorption, scattering and emission rates at all relevant blackbody wavelengths. For this we use the refractive index data plotted in Supplementary Figure 1. Given a spectral rate function $\gamma(\omega)$, which is a dimensionless quantity, the total rate and power are obtained by integrating over all frequencies, $\Gamma = \int_0^\infty \mathrm{d}\omega\,\gamma(\omega)$ and $P = \int_0^\infty \mathrm{d}\omega\,\hbar\omega\gamma(\omega)$.

For absorption and scattering, we assume that the radiation field is in thermal equilibrium at room temperature, $T_\mathrm{env} = 300\,\mathrm{K}$. The absorption of radiation is then proportional to the absorption cross section and to the thermal occupation number, and by integrating over all directions of (isotropic) incident radiation we obtain

$$\gamma_\mathrm{abs}(\omega) = \frac{(\omega/\pi c)^2\,\sigma_\mathrm{abs}(\omega)}{\exp(\hbar\omega/k_B T_\mathrm{env}) - 1} = \frac{4(\omega R/c)^3/\pi}{\exp(\hbar\omega/k_B T_\mathrm{env}) - 1}\mathrm{Im}\left\{\frac{\varepsilon(\omega)-1}{\varepsilon(\omega)+2}\right\}. \qquad \text{(Supplementary Equation 6)}$$

A similar expression holds for the spectral scattering rate,

$$\gamma_{\rm sca}(\omega) = \frac{(\omega/\pi c)^2 \sigma_{\rm sca}(\omega)}{\exp(\hbar\omega/k_B T_{\rm env}) - 1} = \frac{8(\omega R/c)^6/3\pi}{\exp(\hbar\omega/k_B T_{\rm env}) - 1} \left|\frac{\varepsilon(\omega) - 1}{\varepsilon(\omega) + 2}\right|^2 . \qquad \text{(Supplementary Equation 7)}$$

In the case of thermal emission of radiation, we must once again use the absorption cross section. We do, however, allow for a different internal temperature $T_{\rm int}$ of the particle, which may not be in thermal equilibrium with the environment due to trap heating. For all our estimates we consider here the worst-case scenario, where the particle is much hotter than the environment, $T_{\rm int} \gg T_{\rm env}$. In this case there is no stimulated emission by the radiation background and the spectral emission rate is governed by the *Boltzmann* factor [9],

$$\gamma_{\rm emi}(\omega, T_{\rm int}) = \left(\frac{\omega}{\pi c}\right)^2 \sigma_{\rm abs}(\omega) \exp\left(-\frac{\hbar\omega}{k_B T_{\rm int}}\right) = \frac{4}{\pi}\left(\frac{\omega R}{c}\right)^3 \exp\left(-\frac{\hbar\omega}{k_B T_{\rm int}}\right) {\rm Im}\left\{\frac{\varepsilon(\omega) - 1}{\varepsilon(\omega) + 2}\right\}. \qquad \text{(Supplementary Equation 8)}$$

Additional corrections due to the finite heat capacitance of the particle are neglected. Notice the subtle difference between the Planck factor in (Supplementary Equation 6) and the Boltzmann factor in (Supplementary Equation 8), which makes a dramatic difference at low frequencies, $\hbar\omega \ll k_B T_{\rm int,env}$. Whereas the Planck factor gives rise to an enhanced absorption of these low-energy photons, the same photons are emitted from hot particles at a significantly reduced rate due to the lack of stimulated emission [9]. Although this difference has been overlooked in other nanosphere trapping proposals [10, 11], we will see below that this effect can lead to considerable changes in the trap heating rates.

The Boltzmann form (Supplementary Equation 8) ceases to be valid when the internal temperature approaches thermal equilibrium with the environment; it then underestimates the emission rate and, thus, the radiative damping of internal energy. The particle heats up faster and cools down more slowly. Using the above expression can therefore be regarded as a conservative estimate for our reasoning concerning decoherence and heating.

Supplementary Note 2: Dipole trapping, particle size, and initial localization

To achieve significant visibility, we require the position uncertainty of the particle in the trap to be $\sigma_x \lesssim d/(2\pi) \approx 30\,{\rm nm}$. While challenging, this localization is feasible using parametric feedback to 'cool' the center of mass motion of the particle. Employing the method described by Gieseler et al. [12], under the paraxial approximation we find a sensitivity to positional changes of the particle about the center of the trap of $8\alpha/(\epsilon_0 w_0^3 \lambda\sqrt{\pi})$ where w_0 is the waist of the laser spot in which the particle is trapped. The strong dependence upon this waist suggests that a high numerical aperture lens should be used for trapping. Using a numerical aperture of 0.8, one can expect a relative signal change of $2 \times 10^{-8}\ {\rm nm}^{-1}$.

The fractional change in power which one can resolve is ultimately limited by shot noise in the photon number. However, increasing the laser power has the unwanted effect of increasing the trap frequency, and hence increases the bandwidth with which one must resolve this fractional change. Fortunately, the mechanical oscillation can be expected to be characterized by an extraordinarily high Q factor and, by employing boxcar averaging, one may increase the effective integration time.

We choose a mechanical trap frequency of 200 kHz which is similar to previously demonstrated traps and, for silicon, requires a modest 53 mW. For this power, and for a photodiode responsivity of 1.0 A/W, we find a relative shot noise of $1.7 \times 10^{-9}/\sqrt{\rm Hz}$ and thus, using 100 periods for boxcar averaging, a position uncertainty $\sigma_x < 10$ nm can be achieved. The *internal* heating of the particle from photon absorption, as discussed in II, places a limit on the time for which we may trap and implement feedback cooling. For typical values, we anticipate about 10^5 oscillations within which to perform this cooling.

Additionally, since the scattering force causes a size-dependent offset of the equilibrium position from the laser focus, the time-averaged position along the optical axis provides a direct measure of particle size. The particle will be displaced by approximately 10% of its radius and so, by integrating the error signal which we use for feedback over a few hundred milliseconds, we may discern the relative particle size with sub-nanometre precision. The displacement is far more significant at lower NA, to which the trap may be reduced transiently for the express purpose of determining particle size.

Supplementary Note 3: Position stability of the grating

As noted in the main text, the position stability of the grating must be similar to the initial localization of the state σ_x. The positions of the (anti-)nodes in the standing lightwave which forms this grating are fixed relative to

the position of the mirror. Achiving the necessary position stability of this mirror is challenging, but the recently demonstrated 'OTIMA' experiment [13], which employs a similar laser to ionize macro-molecules, has shown that this stability can be achieved when one accounts correctly for the small absorption and consequent heating in the mirrors.

Supplementary Note 4: Position detection and experimentally accessible interferograms

The interferogram is obtained by recording the arrival position of individual nanoparticles on a glass slide at a fixed distance below the source. The position of a nanosphere must be resolved with positional accuracy exceeding $\mu d/3 \sim 100$ nm which, given that one may interrogate individual nanoparticles for an essentially unlimited time, may be achieved by fitting the recorded image to the known point-spread function of the imaging system. For silicon, absorption imaging with visible light can be used. We note that an uncertainty in time t_2 accrues due to the uncertainty in the vertical component of the initial velocity. For the distances in the proposed experiment, we find a relative uncertainty of $\sigma_{t_2}/t_2 \approx 0.5\%$, which is negligibly small.

The experimental apparatus enforces a fixed free-fall distance and limited range over which to vary t_1; hence, rather than directly accessing the fringe pattern as a function of t_2 for fixed t_1 as shown in Fig. 2 of the main text, we instead examine the spatial distribution as a function of the phase modulation parameter ϕ_0, which may be varied by controlling the pulse energy of the grating laser. The corresponding plot is shown in Supplementary Figure 2. When designing the experiment, one is free to choose the free-flight times t_1 and t_2. For a fixed $t_1 = 2t_T$ we plot the expected sinusoidal visibilities, for both quantum and classical cases, as a function of t_2 and of ϕ_0. The resulting surfaces plots are shown in Supplementary Figure 3.

Supplementary Note 5: Internal heating and cooling

We estimate the internal heating of the nanosphere in the trap by solving a rate-balance equation for the internal energy $U(t)$ as a function of time. The energy increases by absorbing either laser photons or blackbody radiation at room temperature, and it decreases by emitting thermal radiation. Given the specific heat c_m of the sphere material, we can identify $\mathrm{d}U/\mathrm{d}t = mc_m \mathrm{d}T_{\mathrm{int}}/\mathrm{d}t$ and write

$$mc_m \frac{\mathrm{d}T_{\mathrm{int}}}{\mathrm{d}t} = \frac{4\pi I_{\mathrm{T}} \omega_{\mathrm{T}} R^3}{c} \mathrm{Im}\left\{\frac{\varepsilon(\omega_{\mathrm{T}}) - 1}{\varepsilon(\omega_{\mathrm{T}}) + 2}\right\} + \int \mathrm{d}\omega \left[\gamma_{\mathrm{abs}}(\omega) - \gamma_{\mathrm{emi}}(\omega, T_{\mathrm{int}})\right] \hbar\omega, \qquad \text{(Supplementary Equation 9)}$$

using the above spectral rate expressions for absorption (Supplementary Equation 6) and emission (Supplementary Equation 8) of thermal radiation. The trap laser intensity and laser frequency are denoted by I_{T} and $\omega_{\mathrm{T}} = 2\pi c/\lambda_{\mathrm{T}}$.

Here, we fix the mechanical trap frequency at $\nu_{\mathrm{M}} = 200\,\mathrm{kHz}$, which requires trapping intensities of $90\,\mathrm{mW}/\mu\mathrm{m}^2$ and $300\,\mathrm{mW}/\mu\mathrm{m}^2$ for 10^6 amu silicon and silica nanospheres, respectively. Assuming a specific heat of $c_m = 700\,\mathrm{J/kg\,K}$ for both materials, and using the interpolated refractive index data of Supplementary Figure 1, a numerical evaluation of (Supplementary Equation 9) yields the heating curves depicted in Supplementary Figure 4. Note that, due to the lack of absorption data at the trap laser wavelength $\lambda_{\mathrm{T}} = 1550\,\mathrm{nm}$ in Ref. [1], we use separate values for the absorption measured in Refs. [2, 3]. They amount to $\mathrm{Im}\{n_{\mathrm{Si}}\} \approx 3.7 \times 10^{-9}$ and $\mathrm{Im}\{n_{\mathrm{SiO2}}\} \approx 2.5 \times 10^{-9}$, and they are included in Supplementary Figure 1.

The striking difference in the heating curves of silicon and silica are due to two reasons: (i) The high refractive index of silicon, $\mathrm{Re}\{n_{\mathrm{Si}}\} = 3.48$ versus $\mathrm{Re}\{n_{\mathrm{SiO2}}\} = 1.44$, which implies less required laser power, i.e. less absorption. (ii) The different absorption spectra in the thermally accessible regime of mid- to far-infrared wavelengths; there, silicon exhibits much less absorption than silica, which inhibits energy damping by emission.

The different thermal emission behavior becomes evident when the particle is released from the trap after a conservatively estimated trapping time of, say, 1000 ms. Supplementary Figure 4 shows the internal temperature of the silicon and silica nanoparticles as a function of time after release. Silicon has a much lower emissivity at thermal infrared wavelengths than silica, which suppresses the emission damping completely over the time scale of the proposed interference experiment. Silica nanoparticles, on the other hand, lose a significant amount of their initial energy. This must be taken into account in the assessment of decoherence by thermal emission of radiation.

III. SUPPLEMENTARY DISCUSSION

State reduction by continuous spontaneous localization (CSL)

The proposed high-mass interferometer scheme can be used to test the predictions of certain macrorealistic collapse models, which were conceived in order to induce a breakdown of the quantum superposition principle and thereby reconcile quantum with classical mechanics at the macroscale [14]. The best studied one is the theory of continuous spontaneous localization (CSL) [15]. The master equation describing the effect of CSL on the center-of-mass motion of a nanoparticle of mass m predicts a fringe reduction equivalent to a decoherence process with the parameters [16, 17]

$$\Gamma_{\mathrm{CSL}} = \left(\frac{m}{1\,\mathrm{amu}}\right)^2 \lambda_{\mathrm{CSL}}, \quad g\left(x\right) = \exp\left(-\frac{x^2}{4r_c^2}\right), \quad f\left(x\right) = \frac{\sqrt{\pi} r_c}{x} \mathrm{erf}\left(\frac{x}{2r_c}\right). \qquad \text{(Supplementary Equation 10)}$$

Here, the CSL localization length is conventionally set to $r_c = 100\,\mathrm{nm}$, and the free rate parameter is currently estimated to be in the range of $\lambda_{\mathrm{CSL}} \sim 10^{-10\pm2}\,\mathrm{Hz}$ [18, 19].

If the CSL effect existed, the sinusoidal fringe visibility Eq. (5) would be reduced by the factor R_1^{CSL}, as obtained by plugging the above CSL parameters into Eq. (6). That is to say, if one would measure at least half of the expected unmodified visibility after $t_1 + t_2 = 3.6 t_T = 284\,\mathrm{ms}$ in the proposed setup, the CSL rate parameter would be bounded by $\lambda_{\mathrm{CSL}} < 1.4 \times 10^{-11}\,\mathrm{Hz}$.

IV. SUPPLEMENTARY METHODS

A. Phase-space description of the interference effect

Next we give a detailed theoretical description of the near-field interference effect discussed in the main text. The model includes the influence of environmental decoherence, an external acceleration, as well as incoherent additions to the grating interaction due to absorption and scattering. The latter are shown to be negligible for the materials considered in the main text, but they may become relevant in other cases.

We treat the problem in one dimension along the grating axis x, where the interference pattern builds up. This assumes that the motional state of the particles along y, z remains separable from the x-motion at all times. In particular, we assume that the grating interaction and the detection do not depend on the y, z-coordinates. In practice, this requires a properly aligned trap (its principal axis parallel to x) and a wide grating laser spot, which guarantees a uniform illumination of the particles irrespectively of their y, z-position.

1. Characteristic function representation

We use the characteristic function representation to conveniently include all decoherence effects and to be able to compare the quantum and the classical expectation within the same formalism. Given the Wigner function $w\left(x,p\right)$ of the one-dimensional motional state of the particle [20], we define the characteristic function as the Fourier transform

$$\chi\left(s,q\right) = \int \mathrm{d}x\mathrm{d}p\, w\left(x,p\right) e^{i(qx-ps)/\hbar} = \mathrm{tr}\left(\rho \exp\left[\frac{i}{\hbar}\left(q\mathsf{x} - \mathsf{p}s\right)\right]\right), \qquad \text{(Supplementary Equation 11)}$$

with x, p the position and momentum operators. The classical analogue, where particles move on ballistic trajectories, is obtained by replacing the Wigner function with the classical phase-space distribution function $f_{\mathrm{cl}}\left(x,p\right)$.

2. Initial state

We start from the motional state of the particle when it is released from the optical trap. To a good approximation, this initial state can be modeled by a thermal harmonic oscillator state. Given the trap frequency ν_{M} and the motional temperature T, the state is represented by the Gaussian Wigner function

$$w_0\left(x,p\right) = \frac{1}{2\pi\sigma_x\sigma_p} \exp\left(-\frac{x^2}{2\sigma_x^2} - \frac{p^2}{2\sigma_p^2}\right), \quad \chi_0\left(s,q\right) = \exp\left(-\frac{\sigma_x^2 q^2 + \sigma_p^2 s^2}{2\hbar^2}\right), \qquad \text{(Supplementary Equation 12)}$$

where the standard deviations in position and momentum read as [20]

$$\sigma_x = \sqrt{\frac{\hbar}{4\pi m\nu_{\mathrm{M}}}\coth\left(\frac{h\nu_{\mathrm{M}}}{2k_BT}\right)}, \qquad \sigma_p = \sqrt{\pi\hbar m\nu_{\mathrm{M}}\coth\left(\frac{h\nu_{\mathrm{M}}}{2k_BT}\right)}. \tag{Supplementary Equation 13}$$

For the realistic values considered here, $\nu_{\mathrm{M}} = 200\,\mathrm{kHz}$ and $T = 20\,\mathrm{mK}$, the Wigner function in (Supplementary Equation 12) is practically indistinguishable from the classical thermal phase-space distribution of the harmonic oscillator, since $h\nu_{\mathrm{M}} \ll k_BT$ and thus $\coth x \approx 1/x$.

On the other hand, if we compare the momentum spread to the elementary momentum unit h/d of the standing-wave grating with $2d = 355\,\mathrm{nm}$, we find $\sigma_p d/h \approx 10^4$. That is, the initial trap state extends over many grating momenta and the time-evolved Gaussian envelope will extend over similarly many grating periods. As long as we are interested in the central part of the interference pattern, where the envelope is flat, it is therefore justified to use the limiting expression

$$\chi_0(s,q) \approx \frac{\sqrt{2\pi}\hbar}{\sigma_p}\exp\left(-\frac{\sigma_x^2q^2}{2\hbar^2}\right)\delta(s)\,, \tag{Supplementary Equation 14}$$

a standard approximation that simplifies the calculation considerably and that is also employed in other near-field interference schemes [8, 21, 22]. Finite-size fringe effects can be disregarded provided the detection window is reasonably small compared to the spread of the final fringe pattern.

3. Free propagation in the presence of acceleration and decoherence

Between the trap , the grating pulse, and the final detection the particle state evolves freely for the times t_1 and t_2. Ideally, this is represented by a shearing transformation of the form $\chi_t(s,q) = \chi_0(s - qt/m, q)$ in phase space [20]. A more realistic assessment must include the influence of possible environmental disturbances as well as inertial forces.

Here, we account for the presence of a (time-dependent) external acceleration $a(t)$, which may be a small component of gravity in the case of grating misalignment, for instance. This yields the Hamiltonian $\mathsf{H}(t) = \mathsf{p}^2/2m + ma(t)\mathsf{x}$ for the one-dimensional motion along the x-axis. The time evolution of the particle's quantum state, $\partial_t\rho = -i[\mathsf{H}(t),\rho]/\hbar + \mathcal{L}(t)\,\rho$, shall include also decoherence effects represented by the (time-dependent) generator $\mathcal{L}(t)$. The latter describes the random unitary state transformation associated to each independent decoherence process: gas collisions, Rayleigh scattering of blackbody photons, and thermal emission or absorption of radiation. Each of these contributes a generator of the form [21]

$$\langle x|\mathcal{L}(t)\,\rho|x'\rangle = \Gamma(t)\left[g(x-x') - 1\right]\langle x|\rho|x'\rangle, \tag{Supplementary Equation 15}$$

in position representation. It describes random jump events $\langle x|\rho|x'\rangle \to g(x-x')\,\langle x|\rho|x'\rangle$ at (possibly time-dependent) rates $\Gamma(t)$. The decoherence function is normalized to $g(0) = 1$, and its characteristic width represents the finite resolution of the decoherence effect. Only those superpositions with a path separation $x - x'$, for which g vanishes approximately, decohere at the full rate $\Gamma(t)$.

In phase space, Eq. (Supplementary Equation 15) is represented by a momentum averaging transformation, which can also be understood in a classical picture. The characteristic function transforms in both the quantum and the classical case as

$$\chi_t(s,q) = \chi_0\left(s - \frac{qt}{m}, q\right)\exp\left\{\frac{i}{\hbar}\left[q\Delta x(t) - \Delta p(t)\,s\right] + \int_0^t \mathrm{d}\tau\,\Gamma(\tau)\left[g\left(s - \frac{q\tau}{m}\right) - 1\right]\right\}. \tag{Supplementary Equation 16}$$

Here, we introduced the momentum and position shifts $\Delta p(t) = m\int_0^t \mathrm{d}t'\,a(t')$ and $\Delta x(t) = \int_0^t \mathrm{d}t'\,\Delta p(t')/m$.

4. Grating transformation

The key difference between the quantum and the classical description of the interferometer is the state transformation at the standing-wave grating. The quantum transformation describes a modulation $\phi(x)$ of the matter-wave phase by the term (Supplementary Equation 3), which leads to interference after the grating. The classical transformation, on the other hand, is given by the accumulated momentum kick $Q(x) = \hbar\partial_x\phi(x)$ exerted on the particle by the dipole force in the standing wave, which leads to a periodic lensing effect after the grating [7].

In phase space, the grating transformation is a convolution, conveniently expressed in terms of the *Talbot* coefficients $B_n(\xi)$ [6, 7, 21],

$$\chi(s,q) \to \sum_n B_n\left(\frac{s}{d}\right)\chi\left(s, q+n\frac{h}{d}\right). \qquad \text{(Supplementary Equation 17)}$$

Here, $d = \lambda_G/2$ denotes the grating period determined by the laser wavelength λ_G. The Talbot coefficients of a standing-wave phase grating assume a simple analytical form in terms of Bessel functions [7], $B_n(\xi) = J_n(\phi_0 \sin \pi\xi)$. The corresponding classical transformation can be brought into the same form (Supplementary Equation 17), substituting $B_n(\xi)$ by their classical counterparts $C_n(\xi) = J_n(\phi_0 \pi \xi)$.

Apart from the coherent phase modulation described by the above grating transformation, random photon absorption and scattering events must also be taken into account. They lead to the following modification of the Talbot coefficients.

Photon absorption transfers momentum in units of the photon momentum $h/2d$ to the particle. This stochastic absorption process is described by the standard master equation [23],

$$\mathcal{L}_{\rm abs}\rho = \gamma_{\rm abs}\left[\cos\left(\frac{\pi \mathsf{x}}{d}\right)\rho\cos\left(\frac{\pi \mathsf{x}}{d}\right) - \frac{1}{2}\left\{\cos^2\left(\frac{\pi \mathsf{x}}{d}\right), \rho\right\}\right], \qquad \text{(Supplementary Equation 18)}$$

which must be added to the coherent time evolution due to the standing-wave field. The absorption rate $\gamma_{\rm abs}$ determines the mean number of absorbed photons, $n_0 = 2\beta\phi_0$, with the parameter β defined in (Supplementary Equation 4) [8].

The master equation $\partial_t \rho = \mathcal{L}_{\rm abs}\rho$ can be integrated explicitly by neglecting the motion during the pulse. The resulting transformation is represented by a convolution in phase space similar to (Supplementary Equation 17), but the Fourier coefficients are now given by modified Bessel functions,

$$R_n^{(\rm abs)}(\xi) = \exp\left(-n_0\frac{1-\cos\pi\xi}{2}\right) I_n\left(n_0\frac{1-\cos\pi\xi}{2}\right). \qquad \text{(Supplementary Equation 19)}$$

Applying both the coherent and the absorption transformation subsequently, we arrive at the overall grating transformation. It is obtained by replacing the coherent Talbot coefficients with

$$B_n(\xi) = e^{-\zeta_{\rm abs}(\xi)}\left[\frac{\zeta_{\rm coh}(\xi)+\zeta_{\rm abs}(\xi)}{\zeta_{\rm coh}(\xi)-\zeta_{\rm abs}(\xi)}\right]^{n/2} J_n\left[\mathrm{sgn}\left\{\zeta_{\rm coh}(\xi)-\zeta_{\rm abs}(\xi)\right\}\sqrt{\zeta_{\rm coh}^2(\xi)-\zeta_{\rm abs}^2(\xi)}\right], \qquad \text{(Supplementary Equation 20)}$$

where we abbreviate $\zeta_{\rm coh}(\xi) = \phi_0 \sin\pi\xi$ and $\zeta_{\rm abs}(\xi) = n_0 \sin^2(\pi\xi/2) = \beta\phi_0(1-\cos\pi\xi)$. The result follows from several steps of calculation using Graf's addition theorem for Bessel functions [24]. Note that the present form differs from the result given in [7], where the absorption effect was described in terms of a classical random walk model. The classical analogue, where the coherent phase modulation is replaced by a position-dependent momentum kick, is obtained by replacing $\zeta_{\rm coh}(\xi)$ with $\phi_0\pi\xi$.

Should Rayleigh scattering be of any concern, one could implement an additional master equation describing the absorption and the subsequent re-emission of laser photons in the form of dipole radiation. A tedious but straightforward calculation would then lead to the modification $B_n(\xi) \to \sum_j B_{n-j}(\xi) R_j(\xi)$, with

$$R_n^{(\rm sca)}(\xi) = \exp\left[-\frac{n_R}{2}\left(1-3\cos\pi\xi\frac{\sin\pi\xi - j_1(\pi\xi)}{2\pi\xi}\right)\right] I_n\left[\frac{n_R}{2}\left(3\frac{\sin\pi\xi - j_1(\pi\xi)}{2\pi\xi} - \cos\pi\xi\right)\right]. \qquad \text{(Supplementary Equation 21)}$$

The mean number of scattered photons, $n_R = 2\eta\phi_0$, is proportional to the material parameter (Supplementary Equation 5).

For the materials considered here, we find $\beta, \eta \ll 1$, and so we neglect the absorption and scattering effect in the main text (although they are included in the simulation). This may no more be the case for other materials or greater masses.

5. *The interference effect*

The interference scheme can now be assessed in phase space using all the above ingredients. The approximate initial state (Supplementary Equation 14) is evolved for the time t_1 after release, using Eq. (Supplementary Equation 16).

Then the grating pulse is applied and the state is propagated for another time t_2. This results in the characteristic function

$$\chi(s,q) = \sum_n B_n\left(\frac{s}{d} - \frac{qt_2}{md}\right)\exp\left\{\frac{i}{\hbar}\left[q\Delta x(t_2) - \Delta p(t_2)\, s\right] + \int_0^{t_2} \mathrm{d}\tau\, \Gamma(t_1+\tau)\left[g\left(s - \frac{q\tau}{m}\right) - 1\right]\right\}$$
$$\times \exp\left\{\frac{i}{\hbar}\left[\left(q + n\frac{h}{d}\right)\Delta x(t_1) - \Delta p(t_1)\left(s - \frac{qt_2}{m}\right)\right] + \int_0^{t_1} \mathrm{d}\tau\, \Gamma(\tau)\left[g\left(s - q\frac{t_2+\tau}{m} - n\frac{h\tau}{md}\right) - 1\right]\right\}$$
$$\times \chi_0\left(s - q\frac{t_1+t_2}{m} - n\frac{ht_1}{md}, q + n\frac{h}{d}\right). \qquad \text{(Supplementary Equation 22)}$$

The density distribution of the particle state, i.e. the interferogram, is obtained by evaluating the integral

$$w(x) = \langle x|\rho|x\rangle = \frac{1}{2\pi\hbar}\int \mathrm{d}q\, \chi_3(0,q)\exp\left(-\frac{iqx}{\hbar}\right)$$
$$= \frac{m}{\sqrt{2\pi}\sigma_p(t_1+t_2)}\sum_n \exp\left[\frac{2\pi i n}{\mu d}(x-\delta x)\right] B_n\left(\frac{nt_2}{\mu t_T}\right)\exp\left\{-\frac{1}{2}\left[\frac{2\pi n\sigma_x t_2}{d(t_1+t_2)}\right]^2\right\}$$
$$\times \exp\left\{\int_0^{t_2} \mathrm{d}\tau\, \Gamma(t_1+\tau)\left[g\left(\frac{nh\tau}{\mu md}\right) - 1\right] + \int_0^{t_1} \mathrm{d}\tau\, \Gamma(\tau)\left[g\left(\frac{nht_2}{\mu md}\frac{t_1-\tau}{t_1}\right) - 1\right]\right\}. \qquad \text{(Supplementary Equation 23)}$$

The Talbot time $t_T = md^2/h$ appears as the natural time scale. We are left with a periodic fringe pattern, where the particle density oscillates at the geometrically magnified grating period $D = \mu d$, with $\mu = (t_1+t_2)/t_1$. In the presence of a time-dependent homogeneous acceleration $a(t)$ the fringe pattern is shifted by

$$\delta x = \Delta x(t_1+t_2) - \mu\Delta x(t_1) = \int_0^{t_1+t_2}\mathrm{d}t\int_0^t \mathrm{d}\tau\, a(\tau) - \mu\int_0^{t_1}\mathrm{d}t\int_0^t \mathrm{d}\tau\, a(\tau)\,. \qquad \text{(Supplementary Equation 24)}$$

In the main text, Eq. (4), we have given the result in the absence of decoherence and acceleration.

In the limit of a perfect point source, $\sigma_x \to 0$, the result is a Talbot-like image of the grating [25], whereas the fringe amplitudes are exponentially reduced for finite σ_x. The fringe pattern washes out completely once $\sigma_x \gtrsim \mu d t_1/2\pi t_2$. The full Talbot effect, i.e. the reconstruction of the grating mask profile (albeit magnified by the factor μ), is observed when t_2/μ is an integer multiple of the Talbot time. In the case of a pure phase grating, however, this reconstruction is a flat line, since $B_n(N\in\mathbb{N}) = \delta_{n,0}$. The classical case is obtained by replacing the Talbot coefficients with their classical counterparts.

Regions of high contrast lie in between the Talbot orders, around $t_2/\mu t_T \approx (2N+1)/2$. At small times $t_2 < t_T$ the quantum and the classical fringe pattern are hard to distinguish. Long flight times, on the other hand, increase the deteriorating influence of decoherence and source averaging. One should therefore generally work in the regime $t_{1,2} \approx t_T$.

Note that the strictly periodic expression (Supplementary Equation 23) for the particle density distribution is only valid for measurements in the center of the Gaussian envelope of the dispersed particle state. The average particle detection probability in a detection window of width W at the center is given by

$$P_{\mathrm{det}} = \langle w(x)\rangle_W \approx \frac{Wm}{\sqrt{2\pi}\sigma_p(t_1+t_2)}. \qquad \text{(Supplementary Equation 25)}$$

B. Influence of decoherence

We now incorporate the four relevant environmental decoherence effects into the calculation. The last line of the expression (Supplementary Equation 23) for the predicted fringe pattern represents the effect of a generic decoherence process of the type (Supplementary Equation 15): it multiplies the fringe amplitudes by the reduction factors

$$R_n = \exp\left\{\int_0^1 \mathrm{d}\vartheta\, \left[t_2\Gamma(t_1+t_2\vartheta) + t_1\Gamma(t_1-t_1\vartheta)\right]\left[g\left(\frac{nht_2\vartheta}{\mu md}\right) - 1\right]\right\}. \qquad \text{(Supplementary Equation 26)}$$

Here, we introduced the dimensionless integration variable ϑ to simplify the according term in (Supplementary Equation 23). We are are left with specifying the rate $\Gamma(t)$ and the decoherence function $g(s)$ for each independent

decoherence process. In all but one case, the decoherence rate will be constant in time and (Supplementary Equation 26) reduces to the simplified form Eq. (6) given in the main text, with $f(s) = \int_0^1 \mathrm{d}\vartheta g(s\vartheta) \in [0,1]$. The latter determines how strongly the decoherence process affects a finite interference path separation on average. The limit, where each scattering event takes away full which-way information, is given by $f(s) = 0$, implying that the matter-wave coherence decays at the maximum rate Γ.

1. Absorption of thermal radiation

Each photon of frequency ω absorbed from the isotropic background radiation field transfers $\hbar\omega/c$ of momentum to the particle. The corresponding decoherence master equation for the reduced one/dimensional state of motion reads as [21]

$$\mathcal{L}_{\mathrm{abs}}\rho = \int \mathrm{d}\omega\, \gamma_{\mathrm{abs}}(\omega) \left[\int_{|\boldsymbol{n}|=1} \frac{\mathrm{d}^2 n}{4\pi} \exp\left(\frac{i\omega n_x \mathsf{x}}{c}\right) \rho \exp\left(-\frac{i\omega n_x \mathsf{x}}{c}\right) - \rho \right], \qquad \text{(Supplementary Equation 27)}$$

with $\gamma_{\mathrm{abs}}(\omega)$ the spectral absorption rate (Supplementary Equation 6). This leads to the decoherence parameters

$$\Gamma_{\mathrm{abs}} = \int \mathrm{d}\omega\, \gamma_{\mathrm{abs}}(\omega), \quad g_{\mathrm{abs}}(x) = \int \frac{\gamma_{\mathrm{abs}}(\omega)\,\mathrm{d}\omega}{\Gamma_{\mathrm{abs}}} \mathrm{sinc}\left(\frac{\omega x}{c}\right), \quad f_{\mathrm{abs}}(x) = \int \frac{\gamma_{\mathrm{abs}}(\omega)\,\mathrm{d}\omega}{\Gamma_{\mathrm{abs}}} \frac{\mathrm{Si}(\omega x/c)}{\omega x/c}. \qquad \text{(Supplementary Equation 28)}$$

2. Emission of thermal radiation

The emission of thermal radiation, the time-reversal of absorption, has the same effect on the motional state of the particle. Assuming an isotropic emission pattern, the same master equation (Supplementary Equation 27) can be used to describe its impact, once the absorption rate is replaced by the spectral emission rate (Supplementary Equation 8) for internally hot particles. If the internal temperature of the particle remains approximately constant the decoherence effect is described by parameters of the same form as (Supplementary Equation 28). If however the particle does cool down significantly during flight, the emission rate will depend on time and the fringe reduction factor becomes

$$R_n^{(\mathrm{emi})} = \exp\left\{ \int \mathrm{d}\omega \int_0^1 \mathrm{d}\vartheta\, \left[t_1 \gamma_{\mathrm{emi}}(\omega, T_{\mathrm{int}}(t_1 - t_1\vartheta)) + t_2 \gamma_{\mathrm{emi}}(\omega, T_{\mathrm{int}}(t_1 + t_2\vartheta)) \right] \left[\mathrm{sinc}\left(\frac{nh\omega t_2}{\mu m c d}\vartheta\right) - 1 \right] \right\}. \qquad \text{(Supplementary Equation 29)}$$

The time dependence of the internal temperature can be estimated by solving the differential equation $mc_m \partial_t T_{\mathrm{int}} = \int \mathrm{d}\omega\, \hbar\omega \left[\gamma_{\mathrm{abs}}(\omega) - \gamma_{\mathrm{emi}}(\omega, T_{\mathrm{int}})\right]$, with c_m the specific heat of the particle material. The solution is plotted in Supplementary Figure 4 for the examples of silicon and silica nanoparticles.

3. Elastic scattering of thermal radiation

Rayleigh scattering of thermal background radiation is governed by the master equation

$$\mathcal{L}_{\mathrm{sca}}\rho = \int \mathrm{d}\omega\, \gamma_{\mathrm{sca}}(\omega) \left\{ \int \frac{\mathrm{d}^2 n \mathrm{d}^2 n'}{16\pi^2} \exp\left[\frac{i\omega(n_x - n_x')\mathsf{x}}{c}\right] \rho \exp\left[\frac{i\omega(n_x' - n_x)\mathsf{x}}{c}\right] - \rho \right\}, \qquad \text{(Supplementary Equation 30)}$$

using the spectral scattering rate (Supplementary Equation 7) and assuming once again an isotropic scattering pattern. This yields the decoherence parameters

$$\Gamma_{\mathrm{sca}} = \int \mathrm{d}\omega\, \gamma_{\mathrm{sca}}(\omega), \quad g_{\mathrm{sca}}(x) = \int \frac{\gamma_{\mathrm{sca}}(\omega)\,\mathrm{d}\omega}{\Gamma_{\mathrm{sca}}} \mathrm{sinc}^2\left(\frac{\omega x}{c}\right), \quad f_{\mathrm{sca}}(x) = \int \frac{\gamma_{\mathrm{sca}}(\omega)\,\mathrm{d}\omega}{\Gamma_{\mathrm{sca}}} \left[\frac{\mathrm{Si}(2\omega x/c)}{\omega x/c} - \mathrm{sinc}^2\left(\frac{\omega x}{c}\right) \right]. \qquad \text{(Supplementary Equation 31)}$$

Our simulations indicate that decoherence by Rayleigh scattering is negligible for the nanospheres considered here, but it will eventually be relevant for larger particles.

4. Collisions with residual gas particles

Collisions with residual gas particles transfers momentum in the same way as elastic light scattering. The corresponding master equation is therefore similar to (Supplementary Equation 30). However, the decoherence function $g_{\mathrm{col}}(s)$ involves the particle-gas scattering amplitudes [21], which we will not evaluate here. Instead, we take the conservative estimate that each collision event transfers sufficiently many grating momenta on average that it fully resolves adjacent interference paths. That is to say, the decoherence function vanishes for $s \neq 0$ and the reduction factor simplifies to $R_n^{(\mathrm{col})} = \exp\left[-\Gamma_{\mathrm{col}}(t_1 + t_2)\right]$.

In order to estimate the effect, we assume that the residual gas of pressure p_g consists of nitrogen ($m_g = 28\,\mathrm{amu}$), in thermal equilibrium with the environment at temperature T_{env}. The mean velocity of the gas particles then reads as $v_g = \sqrt{2k_B T_{\mathrm{env}}/m_g}$. An approximate expression for the total scattering rate is obtained from a van der Waals scattering model [21],

$$\Gamma_{\mathrm{col}} \approx \frac{4\pi\Gamma(9/10)}{5\sin(\pi/5)} \left(\frac{3\pi C_6}{2\hbar}\right)^{2/5} \frac{p_g v_g^{3/5}}{k_B T_{\mathrm{env}}}, \qquad C_6 \approx \frac{3\alpha(\omega=0)\,\alpha_g I_g\, I}{32\pi^2\varepsilon_0^2\,(I+I_g)} \tag{Supplementary Equation 32}$$

where Γ denotes the Gamma function. The van der Waals coupling constant C_6 is estimated by means of the London formula [26], with α, α_g the static polarizabilities and I, I_g the ionization energies of the nanospheres and the gas particles, respectively. For nitrogen, we use $\alpha_g = 1.74\,\mathrm{Å}^3 \times 4\pi\varepsilon_0$ and $I_g = 15.6\,\mathrm{eV}$ [27]. The ionization energy of the nanospheres is roughly estimated by the bulk work function, $I_{\mathrm{Si}}, I_{\mathrm{SiO2}} \approx 5\,\mathrm{eV}$; their static polarizabilities are computed using (Supplementary Equation 1) and assuming static permittivities of $\varepsilon_{\mathrm{Si}} = 11.9$ [28] and $\varepsilon_{\mathrm{SiO2}} = 3.8$ (low-frequency value derived from the spectrum in Supplementary Figure 1).

5. Overall fringe reduction

Finally, the overall fringe reduction factor can be written as

$$\begin{aligned}\ln(R_n) = &-\Gamma_{\mathrm{col}}(t_1+t_2) + \int \mathrm{d}\omega\, \gamma_{\mathrm{abs}}(\omega) \left[\frac{\mathrm{Si}(a_n)}{a_n} - 1\right](t_1+t_2) + \int \mathrm{d}\omega\, \gamma_{\mathrm{sca}}(\omega) \left[\frac{\mathrm{Si}(2a_n)}{a_n} - \mathrm{sinc}^2(a_n) - 1\right](t_1+t_2) \\ &+ \int \mathrm{d}\omega \int_0^1 \mathrm{d}\vartheta\, \left\{t_1 \gamma_{\mathrm{emi}}\left[\omega, T_{\mathrm{int}}(t_1 - t_1\vartheta)\right] + t_2 \gamma_{\mathrm{emi}}\left[\omega, T_{\mathrm{int}}(t_1 + t_2\vartheta)\right]\right\} \left[\mathrm{sinc}(a_n\vartheta) - 1\right],\end{aligned} \tag{Supplementary Equation 33}$$

where we introduced the abbreviation $a_n = nh\omega t_2/\mu mcd$ and Si is the sine integral.

The sinusoidal fringe visibility, Eq. (5) in the main text, is then reduced by the factor R_1. It is plotted in Supplementary Figure 5(a) and (b) as a function of the total time of flight $t_1 + t_2$ and the initial internal temperature $T_{\mathrm{int}}(0)$ for the 10^6 amu silicon and silica nanospheres, respectively. We assume a fixed background pressure of $p_g = 10^{-10}\,\mathrm{mbar}$, where collisional decoherence influences the visibility significantly only after approximately 500 ms.

V. SUPPLEMENTARY REFERENCES

[1] Palik, E. D. & Ghosh, G. *Handbook of optical constants of solids* (Academic press, 1985).

[2] Lee, H., Chen, T., Li, J., Painter, O. & Vahala, K. J. Ultra-low-loss optical delay line on a silicon chip. *Nat. Commun.* **3**, 867 (2012).

[3] Steinlechner, J. *et al.* Optical absorption measurements on crystalline silicon test masses at 1550 nm. *Classical Quant. Grav.* **30**, 095007 (2013).

[4] Kreibig, U. & Vollmer, M. *Optical Properties of Metal Clusters (Springer Series in Materials Science)* (Springer, 1995). URL `http://www.amazon.com/Optical-Properties-Clusters-Springer-Materials/dp/3540578366`.

[5] Berman, P. R. *Atom Interferometry* (Academic Press, San Diego, 1996). URL `http://www.amazon.com/Atom-Interferometry-Paul-R-Berman/dp/0120924609`.

[6] Nimmrichter, S. & Hornberger, K. Theory of near-field matter-wave interference beyond the eikonal approximation. *Phys. Rev. A* **78**, 023612 (2008).

[7] Hornberger, K. *et al.* Theory and experimental verification of Kapitza–Dirac–Talbot–Lau interferometry. *N. J. Phys.* **11**, 043032 (2009).
[8] Nimmrichter, S., Haslinger, P., Hornberger, K. & Arndt, M. Concept of an ionizing time-domain matter-wave interferometer. *N. J. Phys.* **13**, 075002 (2011).
[9] Hansen, K. & Campbell, E. Thermal radiation from small particles. *Phys. Rev. E* **58**, 5477 (1998).
[10] Chang, D. *et al.* Cavity opto-mechanics using an optically levitated nanosphere. *PNAS* **107**, 1005–1010 (2010).
[11] Romero-Isart, O., Juan, M. L., Quidant, R. & Cirac, J. I. Toward quantum superposition of living organisms. *N. J. Phys.* **12**, 033015 (2010).
[12] Gieseler, J., Deutsch, B., Quidant, R. & Novotny, L. Subkelvin Parametric Feedback Cooling of a Laser-Trapped Nanoparticle. *Phys. Rev. Lett.* **109**, 103603 (2012).
[13] Haslinger, P. *et al.* A universal matter-wave interferometer with optical ionization gratings in the time domain. *Nature Physics* **9**, 144–148 (2013).
[14] Bassi, A., Lochan, K., Satin, S., Singh, T. P. & Ulbricht, H. Models of wave-function collapse, underlying theories, and experimental tests. *Rev. Mod. Phys.* **85**, 471–527 (2013). URL `http://link.aps.org/doi/10.1103/RevModPhys.85.471`.
[15] Ghirardi, G. C., Pearle, P. & Rimini, A. Markov processes in Hilbert space and continuous spontaneous localization of systems of identical particles. *Phys. Rev. A* **42**, 78 (1990).
[16] Vacchini, B. On the precise connection between the GRW master equation and master equations for the description of decoherence. *J. Phys. A* **40**, 2463 (2007).
[17] Nimmrichter, S., Hornberger, K., Haslinger, P. & Arndt, M. Testing spontaneous localization theories with matter-wave interferometry. *Phys. Rev. A* **83**, 043621 (2011).
[18] Adler, S. L. Lower and upper bounds on CSL parameters from latent image formation and IGM heating. *J. Phys. A* **40**, 2935 (2007).
[19] Bassi, A., Deckert, D.-A. & Ferialdi, L. Breaking quantum linearity: Constraints from human perception and cosmological implications. *Europhys. Lett.* **92**, 50006 (2010).
[20] Schleich, W. P. *Quantum Optics in Phase Space* (Wiley-VCH, 2001). URL `http://books.google.com/books?id=2jUjQPW-WXAC\&pgis=1`.
[21] Hornberger, K., Sipe, J. & Arndt, M. Theory of decoherence in a matter wave Talbot-Lau interferometer. *Phys. Rev. A* **70**, 053608 (2004).
[22] Juffmann, T., Nimmrichter, S., Arndt, M., Gleiter, H. & Hornberger, K. New prospects for de Broglie interferometry. *Found. Phys.* **42**, 98–110 (2012).
[23] Nimmrichter, S., Hammerer, K., Asenbaum, P., Ritsch, H. & Arndt, M. Master equation for the motion of a polarizable particle in a multimode cavity. *N. J. Phys.* **12**, 083003 (2010).
[24] Abramowitz, M. & Stegun, I. A. (eds.) *Handbook of Mathematical Functions: With Formulas, Graphs, and Mathematical Tables* (Courier Dover Publications, 1965). URL `http://books.google.com/books?id=MtU8uP7XMvoC\&pgis=1`.
[25] Brezger, B., Arndt, M. & Zeilinger, A. Concepts for near-field interferometers with large molecules. *J. Opt. B* **5**, S82 (2003).
[26] London, F. Zur Theorie und Systematik der Molekularkräfte. *Z. Phys.* **63**, 245–279 (1930). URL `http://link.springer.com/10.1007/BF01421741`.
[27] Lide, D. R. (ed.) *CRC Handbook of Chemistry and Physics* (Taylor & Francis Group, 2010), 91st edn.
[28] Young, K. & Frederikse, H. *Compilation of the static dielectric constant of inorganic solids* (American Chemical Society and the American Institute of Physics, 1973).